Mixed-mode delamination of layered structures modeled as Timoshenko beams with linked interpolation

Ranjbar, Maedeh; Škec, Leo; Jelenić, Gordan; Ribarić, Dragan

Source / Izvornik: **International Journal for Numerical Methods in Engineering, 2023, 124, 1773 - 1797**

Journal article, Published version
Rad u časopisu, Objavljena verzija rada (izdavačev PDF)

https://doi.org/10.1002/nme.7187

Permanent link / Trajna poveznica: https://urn.nsk.hr/urn:nbn:hr:157:207585

Received: 3 July 2022 | Revised: 5 December 2022 | Accepted: 5 December 2022

DOI: 10.1002/nme.7187

RESEARCH ARTICLE

WILEY

Mixed-mode delamination of layered structures modeled as Timoshenko beams with linked interpolation

Maedeh Ranjbar | **Leo Škec** | **Gordan Jelenić** | **Dragan Ribarić**

Faculty of Civil Engineering, University of Rijeka, Rijeka, Croatia

Correspondence
Dragan Ribarić, Faculty of Civil Engineering, University of Rijeka, Radmile Matejčić 3, 51000 Rijeka, Croatia.
Email: dragan.ribaric@uniri.hr

Funding information
Hrvatska Zaklada za Znanost, Grant/Award Numbers: IP-2016-06-4775 ASDEL, IP-2018-01-1732 FIMCOS; University of Rijeka, Grant/Award Number: uniri-tehnic-18-248 1415; European Union's Horizon 2020 MSCA-ITN, Grant/Award Number: 860124

Abstract

In this work, a finite-element formulation for modeling mixed-mode delamination in layered structures, consisting of two-node Timoshenko beam finite elements with quadratic linked interpolation and corresponding 4-node interface elements is presented and compared to a more common approach where linear Lagrange interpolation is used. The principal novelty of the proposed approach is that the vertical displacements of the beam elements, as well as the transversal relative displacements of the interface elements, are interpolated using a quadratic linked interpolation that also takes into account the nodal cross-sectional rotations of the beam elements. At the same time, the axial displacements and cross-sectional rotations are interpolated using linear Lagrange polynomials. A bilinear cohesive zone model is embedded in the interface finite elements for delamination modes I and II. Numerical analyses based on the examples from the literature with metal joints show that the formulation with quadratic linked interpolation improves the convergence and robustness of the solution with respect to the approach with linear interpolation. On the other hand, in case of composites with stiff adhesives this formulation exhibits a peculiar behavior with spurious oscillations of the normal interface tractions that leads to a poor performance in mode-I and mixed-mode tests. This problem can be easily solved by canceling the quadratic term in the interpolation function and using the standard Lagrange interpolation in such cases.

KEYWORDS

cohesive-zone model, delamination, finite-element analysis, interface element, linked interpolation, Timoshenko beam theory

1 | INTRODUCTION

Composite structures are nowadays widely used in the industry, from aerospace and automotive, to electronics and medicine. The interface between components is often the weakest part of the structure, which is why special attention must be dedicated not only to the design of individual components, but also to the design of their interconnection. In general, the interconnection between the components can be continuous (adhesives) or discrete (shear connectors) and although both of these types have a wide range of applicability, in this work we will focus only on continuous interfaces.

For practical reasons, it is also common to model discrete connectors as a "smeared" continuous interface,[1,2] which is defined by their individual compliance (slip modulus).[3] Delamination, which is how the loss of interconnection between the components is usually called, is the most common and severe failure mode in composites.

Understanding and modeling fracture of materials has been an extremely active research topic for almost a century. Development of linear-elastic fracture mechanics (LEFM), thanks to the pioneering work of Griffith[4] and Irwin,[5] has provided relatively simple tools for characterizing fracture resistance of structures that have been extensively used in research and industry ever since. In fact, essentially all current industrial standards[6-8] used to characterize fracture resistance of composites and adhesive joints are based on LEFM and its key parameter—the critical energy release rate (G_c). On the other hand, LEFM assumes an infinite stress at the crack tip,[9] as a consequence of the very simple model of fracture. In reality, during crack propagation, most materials will exhibit nonlinear material behavior in a zone of finite length in front of the crack tip, called the damage-process zone (DPZ). In this zone, before total failure of a material, its bearing capacity will be progressively lost, which is known as material softening.

Cohesive zone models (CZMs) are nowadays among the most popular tools for modeling crack propagation with progressive damage, that is, with a DPZ developed in front of the crack tip. Based on the strip-yield model proposed by Dugdale[10] and Barenblatt[11] in 1960s, the first implementation of CZMs within the finite-element framework is attributed to Hillerborg and his co-workers in 1976.[12] Since then, there has been a rapid development of various types of CZMs and today cohesive elements are a standard part of finite-element libraries of most popular commercial software packages for structural analysis. Each CZM is defined by its traction-separation law (TSL), that is, the relationship between the relative displacement of the crack faces and the corresponding stress.

In the framework of finite element analysis (FEA), CZMs are usually embedded in so-called interface elements. These elements are then placed at the interfaces between solid finite elements where the crack is expected to propagate and attached to their nodes. In a 2D analysis, the interface between solid elements is a line where only normal and sliding shear relative displacements can occur. In a 3D problem, the interface between solid finite elements is a plane, where in general all three modes of delamination are possible. In many situations (such as standard delamination tests[6-8]), however, out-of-plane effects can be neglected and, for the sake of reducing the computational burden, such simulations are usually performed using 2D models, where the third mode of delamination (scissoring shear) is excluded. Regardless of whether the analysis is 2D or 3D, the interface elements with embedded CMZs introduce material nonlinearity in the numerical model of the type that often causes convergence problems and requires more advanced and robust solution algorithms.[13-15] In front of the crack tip, the resulting distribution of interface tractions is highly nonlinear and can include a transition from tensile to compressive tractions over a very small distance. In turn, extremely fine meshes around the crack tip are required in some cases and, because the crack tip travels during delamination, this can significantly increase the computational time required to complete the simulation with a sufficiently accurate (smooth) solution. In order to avoid this problem, several solutions have been proposed in the literature that include adjusting the interface parameters,[16,17] adaptive integration schemes,[18-20] and different enrichment of elements.[21-23] Therefore, successful numerical modeling of delamination is a nontrivial task, even using a commercial software.

To reduce the computational cost, instead of more complex 2D solid finite-element models with interface elements, delamination problems can be modeled by combining *beam finite elements* with interface elements, which use less degrees of freedom and possibly provide a more robust solution.[24] An analogous approach in 3D has been employed by Dávila et al.,[25] where instead of 3D solid elements, shell elements have been used to model the layers.

Because the nodes of beam finite elements are usually located on the centroidal axis and the interface between components is located on the beam edges (top or bottom), the relative displacements at the interface must be computed by taking into account the distance from the reference axis to the edge of the beam and the beam's cross sectional rotations. Therefore, such interface elements must have different degrees of freedom than the standard interface elements used in conjunction with 2D or 3D solid finite elements. If one wants to exploit the advantages of commercial FEA software infrastructure for 2D delamination analyses using beam finite elements, modified interface elements have to be developed and implemented in the software.

As shown in Reference 26, a way to get around this issue can be found in locating the reference axis (or plane in case of plates) at the edge of the elements, so that the influence of the cross-sectional rotations on the relative displacements at the interface is excluded. However, this approach has two main drawbacks. First, it is not applicable to problems that involve more than two layers, that is, the layers that have interfaces at both edges. Second, as reported in Reference 24, moving the beam's reference axis away from the centroidal line decrease accuracy and robustness of the simulation.

Instead of giving a general mathematical formulation of a stack of alternating beam and interface elements, effectively producing a macro-element with a number of degrees of freedom (DOFs) dependent on the number of layers,[24] Russo

and Chen[20] implemented an independent interface element that can be connected to Euler–Bernoulli (EB) beam finite elements. They confirmed and additionally elaborated the benefits of modeling delamination using beam finite elements previously reported in References 15 and 24.

When shear modulus of the layers is relatively low, which is often the case for orthotropic materials such as composite laminates,[16,27,28] accounting for shear deformability of the layers becomes increasingly important. In that respect, the shear-deformable Timoshenko beam (TB) finite elements possess an obvious advantage over the EB elements. In particular, it has been shown in Reference 29 that the EB beam solution overestimates the peak load in the load-displacement curve of a double-cantilever beam (DCB) test. This effect is obviously not desirable in the design of composite structures, especially so since it amplifies as the interface becomes stiffer.

One aim of this article is to present the manner in which the approach presented in Reference 24 may be applied to derive an independent interface element, rather than a macro-element composed of layers and interfaces, then facilitating implementation into existing finite-element codes. More importantly, the article is set to analyse the performance of the TB elements with the so-called linked interpolation, in which the transversal displacement field depends not only on the nodal displacements, but also on the nodal rotations. This interpolation has been successfully applied to beams (e.g., References 30-34 and the references therein) and plates (e.g., References 35 and 36 and the references therein), but to the best of our knowledge, not to the problem of delamination in which the layers are modeled as beams or plates. Specifically, we limit our attention to two-node TB elements (TB2), whereby the linked interpolation enables a quadratic, rather than only linear, interpolation of the displacement field and investigate the effect of slope discontinuity on the mode I, mode II and I+II delamination problems involving bilinear cohesive zone interface model. This discontinuity is standard in the TB elements (with and without linked interpolation) and beneficial for the accurate description of shear in the presence of concentrated forces and reactions. Here we investigate its effect in delamination, where such concentrated effects are absent and assess the benefits of linked interpolation.

An important point to note is that in a conformal finite-element setting, the edges of an interface element should displace exactly as the edges of the layers between which the interface is sandwiched, which depends on the displacement interpolation used in the beam layer, possibly linked, and the offset between the layer edge and the corresponding reference line. The interface element therefore, involves not only the nodal displacements, but also the nodal rotations.

The article is organized as follows. In Section 2, the formulation of the 4-node interface element with Timoshenko-beam quadratic linked interpolation is given, along with all relevant details for the numerical implementation. In Section 3, the performance of the proposed finite-element model is assessed using delamination tests in mode-I, mode-II, and mixed-mode (I+II) and compared with an analogous model that uses standard linear Lagrange interpolated elements interpolation. Finally, in Section 4, conclusions are drawn and guidelines for the future work given.

2 | FE IMPLEMENTATION OF THE BEAM-LINKED INTERFACE ELEMENT

A sample 4-node interface element attached to the nodes of two adjacent two-node beam finite elements and the corresponding degrees of freedom in each node are shown in Figure 1. Although in this figure, a small gap is depicted between the layers, in the present work it will be assumed that the interface between components has zero thickness, which is a common approach.[16] Moreover, it can be easily shown[15] that for this type of interface elements, the relative displacements at the interface, and therefore the stresses transmitted between the components, are independent of the thickness of the interface. In this work, we will denote as BINT4 the interface element that can be used in conjunction with two-node beam finite elements, where "B" stands for "beam," "INT" for "interface" and "4" is the element's number of nodes. This follows the notation INT4 that is commonly used for 4-node interface elements that are used with 2D-solid finite elements.

The vector of relative displacements at the actual interface can be written as

$$\boldsymbol{\delta} = \begin{Bmatrix} \delta_{\mathrm{I}} \\ \delta_{\mathrm{II}} \end{Bmatrix} = \begin{Bmatrix} v_b - v_a \\ u_b - u_a + \frac{h_a}{2}\theta_a + \frac{h_b}{2}\theta_b \end{Bmatrix}, \tag{1}$$

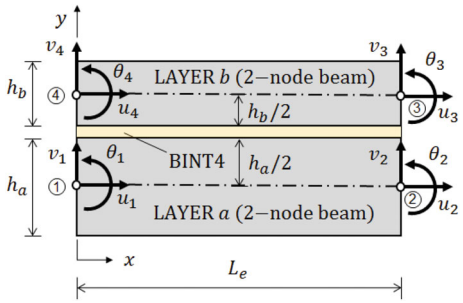

FIGURE 1 BINT4 interface element attached to nodes of two-node beam finite elements

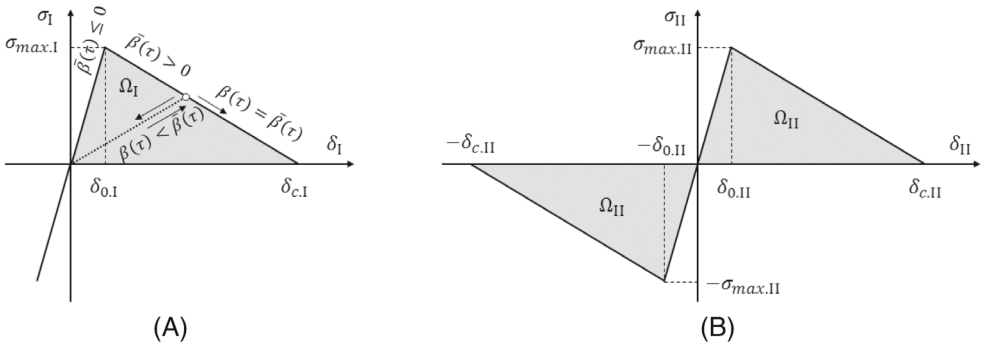

FIGURE 2 Bi-linear traction-separation law in (A) mode I and (B) mode II

where the components δ_{I} and δ_{II} correspond to modes I and II, respectively. The horizontal and vertical displacements of the layers' reference axes, and their cross-sectional rotations are denoted as u_i, v_i, and θ_i $(i = a, b)$, respectively. Here it is assumed that the reference axis of each layer corresponds to its centroidal line located at layer's middle height.

2.1 | Formulation of the residual vector

The internal virtual work of the interface element is defined as

$$V_{int} = w \int_{L_e} \overline{\boldsymbol{\delta}} \cdot \boldsymbol{\sigma} \mathrm{d}x, \tag{2}$$

where w is the width of the interface, $\overline{\boldsymbol{\delta}}$ is the vector of virtual relative displacements at the interface, and $\boldsymbol{\sigma}$ is the vector of stresses (tractions) at the interface. Note that both $\overline{\boldsymbol{\delta}}$ and $\boldsymbol{\sigma}$ have two components, one for each delamination mode. The relationship between the stresses and the relative displacements at the interface is defined by a bilinear TSL, as depicted in Figure 2.

In mode I no softening (damage) can occur in compression, while in mode II the behavior is independent of the direction (or the sign) of the relative displacement. The principal parameters of the bilinear TSL are the maximum traction (stress) at the interface $\sigma_{\max .i}$ and the corresponding relative displacement $\delta_{0.i}$, as well as the relative displacement corresponding to the complete failure $\delta_{c.i}$, where i = I,II refers to the mode of delamination. The area under the TSL represents the work of separation and it is denoted by Ω_i. As explained in more detail in Reference 37, the work of separation of a CZM is equal to the critical value of the J integral and, only in case of steady-state crack propagation, it is also equal to the LEFM critical energy release rate (G_c).

Note that the CZM for mode II (Figure 2B) does not account for friction on the crack surfaces, which is typical for end-notch flexure (ENF) tests. Although several authors proposed CZMs that could take into account this effect,[38-40] in the present work such an approach is avoided for the sake of simplicity and clarity because the focus is on the comparison

of different interpolation functions for TB finite elements. Such a simplified, but yet commonly used approach proved to be sufficiently accurate for the examples analysed in the present work.

To model the irreversibility of damage, a damage-history variable $\overline{\beta}$ is introduced in the model as

$$\overline{\beta}(\tau) = \max_{0 \le \tau' \le \tau} \beta(\tau'), \tag{3}$$

where τ represents pseudo-time and β is defined as[16]

$$\beta = \sqrt{\left(\frac{\langle \delta_{\mathrm{I}} \rangle}{\delta_{0.\mathrm{I}}}\right)^2 + \left(\frac{|\delta_{\mathrm{II}}|}{\delta_{0.\mathrm{II}}}\right)^2} - 1. \tag{4}$$

Note that in $\langle \delta_{\mathrm{I}} \rangle$ Macaulay brackets are used so that in case of compression ($\delta_{\mathrm{I}} < 0$) this term is equal to zero and no damage is produced in mode I. In the initial (undeformed) stage, where $\delta_{\mathrm{I}} = \delta_{\mathrm{II}} = 0$, we have $\beta = -1$. Equation (4) introduces a proper coupling of modes in the model, where both modes contribute to the value of the common damage parameter $\overline{\beta}$. Taking into account the damage history, the tractions at the interface can be written as

$$\boldsymbol{\sigma} = \begin{cases} \boldsymbol{S\delta}, & \text{for } \overline{\beta} \le 0, \\ (\boldsymbol{I}_2 - \boldsymbol{D})\boldsymbol{S\delta}, & \text{for } \overline{\beta} > 0, \end{cases} \tag{5}$$

where for $k_i = \sigma_{\max .i}/\delta_{0.i}$ $(i = \mathrm{I,II})$

$$\boldsymbol{S} = \begin{bmatrix} k_{\mathrm{I}} & 0 \\ 0 & k_{\mathrm{II}} \end{bmatrix}, \tag{6}$$

$\boldsymbol{I}_2$ is the 2×2 identity matrix,

$$\boldsymbol{D} = d \begin{bmatrix} \langle \mathrm{sgn}(\delta_{\mathrm{I}}) \rangle & 0 \\ 0 & 1 \end{bmatrix}, \quad d = \min \left\{ 1, \frac{1}{1-\alpha} \frac{\overline{\beta}}{1+\overline{\beta}} \right\} \tag{7}$$

and

$$\alpha = \frac{\delta_{0.\mathrm{I}}}{\delta_{c.\mathrm{I}}} = \frac{\delta_{0.\mathrm{II}}}{\delta_{c.\mathrm{II}}}. \tag{8}$$

The first case in Equation (5) ($\overline{\beta} \le 0$) corresponds to the undamaged (linear-elastic) state and the second case ($\overline{\beta} > 0$) to the damaged state, where the initial stiffness of the interface $\boldsymbol{S}$ is reduced by the nonzero damage matrix $\boldsymbol{D}$. Obviously, total damage of the interface will occur when $\boldsymbol{D} = \boldsymbol{I}_2$ and from Equation (7) it can be noted that the coupled damage parameter $\overline{\beta}$ is indeed used for both modes. To keep the same level of damage in both modes in Equation (7), parameter α is introduced in Equation (8), where $\alpha \in \langle 0, 1 \rangle$. This is important because in a case where $\delta_{0.\mathrm{I}}/\delta_{c.\mathrm{I}} \neq \delta_{0.\mathrm{II}}/\delta_{c.\mathrm{II}}$, there would be two different values of d for each mode in Equation (7), which would allow to reach complete debonding of one point of the interface at two different times for modes I and II. In other words, it would be possible to reach complete debonding only in one mode, while transmitting interface tractions in the other mode, which is physically inconsistent (for more details about this issue, see Reference 16).

Note that for limit cases with $\delta_{\mathrm{I}} = \delta_{0.\mathrm{I}}$ and $\delta_{\mathrm{II}} = 0$ (pure mode I) or $\delta_{\mathrm{I}} = 0$ and $\delta_{\mathrm{II}} = \delta_{0.\mathrm{II}}$ (pure mode II) according to Equation (4) $\beta = 0$, which in Equation (7) will result in no damage at the interface ($\boldsymbol{D} = \boldsymbol{O}$). However, if the two limit cases are combined in a way that $\delta_{\mathrm{I}} = \delta_{0.\mathrm{I}}$ and $\delta_{\mathrm{II}} = \delta_{0.\mathrm{II}}$, according to Equation (4) $\beta = \sqrt{2} - 1$ and from Equation (7) $d > 0$ and at least one member of matrix $\boldsymbol{D}$ is greater than zero. This means that, although in individual modes there is no softening (damage), their combination in a coupled damage law results in damage that affects interface tractions in both modes, as it can be seen in Equation (5). It follows that damage at the interface can occur also for cases with $\delta_{\mathrm{I}} < \delta_{0.\mathrm{I}}$ and $\delta_{\mathrm{II}} < \delta_{0.\mathrm{II}}$.

Note also that $\langle \mathrm{sgn}(\delta_{\mathrm{I}}) \rangle$ is used in $\boldsymbol{D}$ to assure that the compressive stiffness of the interface in mode I (defined by k_{I}) is not reduced in case when damage occurs only in mode II. This feature is extremely important for standard mode-II tests

such as ENF[7] or end-loaded split (ELS),[41] where pure mode-II conditions are obtained by creating compression at the interface. Therefore, from Equation (7) it clearly follows that, except in compression, the damage is mode independent.

Following Equation (1), the vector of virtual relative displacements can be written as

$$\overline{\boldsymbol{\delta}} = \boldsymbol{B}\,\overline{\boldsymbol{p}}, \tag{9}$$

where

$$\boldsymbol{B} = \begin{bmatrix} 0 & -1 & 0 & 0 & 1 & 0 \\ -1 & 0 & \frac{h_a}{2} & 1 & 0 & \frac{h_b}{2} \end{bmatrix} \tag{10}$$

and

$$\overline{\boldsymbol{p}} = \langle\, \overline{u}_a \quad \overline{v}_a \quad \overline{\theta}_a \quad \overline{u}_b \quad \overline{v}_b \quad \overline{\theta}_b \,\rangle^{\mathsf{T}}. \tag{11}$$

The unknown functions contained in vector $\overline{\boldsymbol{p}}$ are interpolated as

$$\overline{\boldsymbol{p}} = \boldsymbol{P}\,\overline{\boldsymbol{p}}_N, \tag{12}$$

where $\boldsymbol{P}$ is the matrix of interpolation functions and $\overline{\boldsymbol{p}}_N$ is the vector of nodal degrees of freedom. Because two-node beam finite elements are used in conjunction with BINT4 interface elements, we have

$$\boldsymbol{P} = \begin{bmatrix} \boldsymbol{\Psi}_1 & \boldsymbol{\Psi}_2 & \mathbf{0}_3 & \mathbf{0}_3 \\ \mathbf{0}_3 & \mathbf{0}_3 & \boldsymbol{\Psi}_2 & \boldsymbol{\Psi}_1 \end{bmatrix}, \tag{13}$$

where $\boldsymbol{\Psi}_i$ $(i = 1, 2)$ are 3×3 matrices containing interpolation functions and $\mathbf{0}_3$ is the 3×3 zero matrix. As mentioned earlier, interpolation functions used in the interface elements are inherited from the adjacent beam finite elements. In this article, we specifically address the second-order linked interpolation for TB2[42] of length L_e which reads

$$u = \psi_1 u_1 + \psi_2 u_2, \tag{14}$$

$$v = \psi_1 v_1 + \psi_2 v_2 + \frac{L_e}{2}\psi_1\psi_2(\theta_1 - \theta_2), \tag{15}$$

$$\theta = \psi_1\theta_1 + \psi_2\theta_2, \tag{16}$$

where for the nodal values of displacements and cross-sectional rotations indices 1 and 2 refer to the left- and right-hand node of the beam element, respectively, while the interpolation functions are defined as

$$\psi_1 = \psi_1(x) = 1 - \frac{x}{L_e} \quad \text{and} \quad \psi_2 = \psi_2(x) = \frac{x}{L_e}. \tag{17}$$

It can be noticed that the only part that distinguishes such an interpolation from the standard linear Lagrange interpolation, is the quadratic term $L_e\psi_1\psi_2(\theta_1 - \theta_2)/2$ in Equation (15). It is therefore convenient to decompose the interpolation-function matrices $\boldsymbol{\Psi}_i$ of the interface element from Equation (13) into linear and quadratic part as

$$\boldsymbol{\Psi}_i = \boldsymbol{\Psi}_{i.L} + \boldsymbol{\Psi}_{i.Q}, \quad i = 1, 2, \tag{18}$$

where the linear part, $\boldsymbol{\Psi}_{i.L} = \psi_i \boldsymbol{I}_3$, is the product of the first-order Lagrange interpolation functions given in Equation (17) and the 3×3 identity matrix $\boldsymbol{I}_3$, while the quadratic part, $\boldsymbol{\Psi}_{i.Q}$, reads

$$\boldsymbol{\Psi}_{i.Q} = (-1)^{(i-1)} \begin{bmatrix} 0 & 0 & 0 \\ 0 & 0 & \frac{L_e}{2}\psi_1\psi_2 \\ 0 & 0 & 0 \end{bmatrix}. \tag{19}$$

Note that by setting $\boldsymbol{\Psi}_{i.Q} = \mathbf{0}_3$, the formulation (18) reduces to the standard linear Lagrange interpolation.

According to Figure 1, nodal degrees of freedom can be collected as

$$\boldsymbol{p}_N = \langle\, u_1 \quad v_1 \quad \theta_1 \quad u_2 \quad v_2 \quad \theta_2 \quad u_3 \quad v_3 \quad \theta_3 \quad u_4 \quad v_4 \quad \theta_4 \,\rangle^{\mathsf{T}}, \tag{20}$$

while $\overline{\boldsymbol{p}}_N$ is obtained analogously using virtual nodal displacement and rotations. Substituting (12) in (9) yields

$$\overline{\boldsymbol{\delta}} = \boldsymbol{B}\,\boldsymbol{P}\,\overline{\boldsymbol{p}}_N = \boldsymbol{Y}\,\overline{\boldsymbol{p}}_N, \tag{21}$$

where

$$\boldsymbol{Y} = \begin{bmatrix} 0 & -\psi_1 & -\frac{L_e}{2}\psi_1\psi_2 & 0 & -\psi_2 & \frac{L_e}{2}\psi_1\psi_2 & 0 & \psi_2 & -\frac{L_e}{2}\psi_1\psi_2 & 0 & \psi_1 & \frac{L_e}{2}\psi_1\psi_2 \\ -\psi_1 & 0 & \frac{h_a}{2}\psi_1 & -\psi_2 & 0 & \frac{h_b}{2}\psi_2 & \psi_2 & 0 & \frac{h_a}{2}\psi_2 & \psi_1 & 0 & \frac{h_b}{2}\psi_1 \end{bmatrix}, \tag{22}$$

which for the standard linear Lagrange interpolation, after canceling the second-order terms, becomes

$$\boldsymbol{Y} = \begin{bmatrix} 0 & -\psi_1 & 0 & 0 & -\psi_2 & 0 & 0 & \psi_2 & 0 & 0 & \psi_1 & 0 \\ -\psi_1 & 0 & \frac{h_a}{2}\psi_1 & -\psi_2 & 0 & \frac{h_b}{2}\psi_2 & \psi_2 & 0 & \frac{h_a}{2}\psi_2 & \psi_1 & 0 & \frac{h_b}{2}\psi_1 \end{bmatrix}. \tag{23}$$

It is worth noting that using the quadratic linked interpolation in the BINT4 element makes difference with respect to using the linear interpolation only for the opening mode, while for the shearing mode (see how δ_{II} is defined in Equation (1)), they are identical.

Finally, Equation (2) becomes

$$V_{int} = \overline{\boldsymbol{p}}_N^{\mathsf{T}}\, w \int_{L_e} \boldsymbol{Y}^{\mathsf{T}}\boldsymbol{\sigma}\, \mathrm{d}x, \tag{24}$$

from where it follows that the vector of internal forces of the interface is

$$\boldsymbol{q}_{int} = w \int_{L_e} \boldsymbol{Y}^{\mathsf{T}}\boldsymbol{\sigma}\, \mathrm{d}x. \tag{25}$$

In TB theory, the cross-sectional rotation is the difference between the slope of the reference axis (the first derivative of the transversal displacement) and the shear strain, that is

$$\theta = v' - \gamma. \tag{26}$$

By substituting interpolation functions (14)–(17) in Equation (26), we can show that the shear strains have a constant value

$$\gamma = \frac{v_2 - v_1}{L_e} - \frac{\theta_1 + \theta_2}{2} \tag{27}$$

along an element. Obviously, at the nodes shared by adjacent elements, the shear strains (and shear forces) will be in general discontinuous. Because cross-sectional rotations θ are continuous at the nodes, from Equation (26) it follows that the slope of the beam's reference axis (v') will be also discontinuous at the nodes. We will refer to this feature when analyzing the results of simulations in Section 3.2. Discontinuity of v' and γ is also present in linear two-node TB elements, where, in contrast to the quadratic linked interpolation employed, v' is constant, while γ has a linear distribution along an element.

2.2 | Formulation of the stiffness matrix

The stiffness matrix of the interface element is obtained by linearising its vector of internal forces with respect to the nodal values of the unknown functions. Thus, in Equation (25) only $\boldsymbol{\sigma}$ needs to be linearized using

$$\Delta\boldsymbol{\sigma} = \begin{cases} \boldsymbol{S}\Delta\boldsymbol{\delta}, & \text{for } \overline{\beta} \le 0, \\ -\Delta\boldsymbol{D}\boldsymbol{S}\boldsymbol{\delta} + (\boldsymbol{I}_2 - \boldsymbol{D})\boldsymbol{S}\Delta\boldsymbol{\delta}, & \text{for } \overline{\beta} > 0. \end{cases} \tag{28}$$

According to Equation (21), it follows that

$$\Delta\boldsymbol{\delta} = \boldsymbol{Y}\Delta\boldsymbol{p}_N, \tag{29}$$

where $\Delta\boldsymbol{p}_N$ is obtained from (20). Because $\overline{\beta}$ is a function of the current (at pseudo-time τ) nodal values of the unknown functions only if the damage is progressing, that is, when $\beta(\tau) = \overline{\beta}(\tau)$, $\Delta\boldsymbol{D}$ can be written as

$$\Delta\boldsymbol{D} = \begin{cases} \boldsymbol{0}, & \text{for } \beta(\tau) < \overline{\beta}(\tau), \\ \Delta d \begin{bmatrix} \langle \mathrm{sgn}(\delta_{\mathrm{I}}) \rangle & 0 \\ 0 & 1 \end{bmatrix}, & \text{for } \beta(\tau) = \overline{\beta}(\tau). \end{cases} \tag{30}$$

It can be easily shown that

$$\Delta d = \begin{cases} \dfrac{1}{1-\alpha}\dfrac{1}{(1+\overline{\beta})^3}\boldsymbol{\eta}^{\mathsf{T}}\Delta\boldsymbol{\delta}, & \text{for } d < 1, \\ 0, & \text{for } d = 1, \end{cases} \tag{31}$$

where α is defined in (8) and

$$\boldsymbol{\eta}^{\mathsf{T}} = \begin{bmatrix} \left(\dfrac{\langle\delta_{\mathrm{I}}\rangle}{\delta_{0.\mathrm{I}}}\right)^2 \dfrac{1}{\delta_{\mathrm{I}}} & \left(\dfrac{|\delta_{\mathrm{II}}|}{\delta_{0.\mathrm{II}}}\right)^2 \dfrac{1}{\delta_{\mathrm{II}}} \end{bmatrix}. \tag{32}$$

Equation (28) can be now rewritten as $\Delta\boldsymbol{\sigma} = \boldsymbol{U}\Delta\boldsymbol{\delta}$, where

$$\boldsymbol{U} = \begin{cases} \boldsymbol{S}, & \text{for } \overline{\beta}(\tau) \le 0, \\ (\boldsymbol{I}_2 - \boldsymbol{D})\boldsymbol{S}, & \text{for } \beta(\tau) < \overline{\beta}(\tau), \\ (\boldsymbol{I}_2 - \boldsymbol{D})\,\boldsymbol{S} - \boldsymbol{J}\,\boldsymbol{S}\,\boldsymbol{\delta}\,\boldsymbol{\eta}^{\mathsf{T}}, & \text{for } \beta(\tau) = \overline{\beta}(\tau), \end{cases} \tag{33}$$

with

$$\boldsymbol{J} = j \begin{bmatrix} \langle \mathrm{sgn}(\delta_{\mathrm{I}}) \rangle & 0 \\ 0 & 1 \end{bmatrix}, \quad j = \frac{1}{1-\alpha}\frac{\mathrm{sgn}(1-d)}{(1+\overline{\beta})^3}, \quad i = \mathrm{I,II}. \tag{34}$$

Matrix $\boldsymbol{U}$ in Equation (33) represents the stiffness of the interface with three possible cases, which is also indicated in Figure 2A. The first case ($\overline{\beta}(\tau) \le 0$) corresponds to the undamaged (linear-elastic) behavior, the second case ($\beta(\tau) < \overline{\beta}(\tau) > 0$) is the secant stiffness that is used in case of unloading, while the third case ($\beta(\tau) = \overline{\beta}(\tau) > 0$) gives the tangent stiffness in the case of progressing damage. Note that the first two cases give positive stiffness, while the third gives a negative stiffness (softening). When the interface is completely damaged ($d_i = 0, i = \mathrm{I, II}$), the stiffness in both the second and the third case is zero.

Finally, linearized equation (25) can be written as

$$\Delta\boldsymbol{q}_{int} = w\int_{L_e} \boldsymbol{Y}^{\mathsf{T}}\boldsymbol{U}\boldsymbol{Y}\Delta\boldsymbol{p}_N \mathrm{d}x, \tag{35}$$

from where the stiffness matrix follows as

$$\boldsymbol{K} = w \int_{L_e} \boldsymbol{Y}^{\mathrm{T}} \boldsymbol{U} \boldsymbol{Y} \mathrm{d}x. \tag{36}$$

It is worth noting that the vector of internal forces and the stiffness matrix given in Equations (25) and (36), respectively, can be considered as general expressions in which $\boldsymbol{\sigma}$ and $\boldsymbol{U}$ change depending on the type of the CZM, while the change of interpolation functions only affects the matrix $\boldsymbol{Y}$.

For numerical integration of the residual vector and stiffness matrix, the Newton–Cotes method proposed in Reference 16 is used with three and five integration points for the linear and quadratic elements, respectively, which in both cases is sufficient to correctly evaluate the integral appearing in the stiffness matrix (Equation 36) once all integration points within a single element have the same stiffness value (either positive or negative). Improved stress integration schemes (e.g., adaptive integration[18] or subdomain integration[43]) can be used for an accurate integration in elements where the stiffness changes. For example, when the bilinear CZM is used in pure mode I, there are two such partially damaged elements, one containing the relative displacement $\delta_{0,\mathrm{I}}$ and the other $\delta_{c,\mathrm{I}}$. Integration of such elements can be associated with high error if not very small elements or higher-order integration is used. Nevertheless, in this work the performance of different integration schemes has not been analyzed to facilitate the comparison of the proposed model with that using linear interpolation functions.

2.3 | Solution procedure

The global vector of residual forces is computed as $\boldsymbol{g}_G = \boldsymbol{q}_{\mathrm{int}.G} - \boldsymbol{q}_{\mathrm{ext}.G}$, where the contribution of the interface (25) to the vector of internal forces $\boldsymbol{q}_{\mathrm{int}.G}$ is simply added to the nodes shared between the beam and the interface elements. In a similar fashion, contribution (36) is added to the global stiffness matrix of the system $\boldsymbol{K}_G$. Finally, the global system $\Delta \boldsymbol{p}_G = -\boldsymbol{K}_G^{-1} \boldsymbol{g}_G$ is solved iteratively to obtain the updated nodal values of displacements and rotations. It is worth noting that in the first iteration of each increment, the tangent predictor procedure is adopted in line with the strategy proposed in Reference 16, that is, in the first iteration in each increment, only further delamination is allowed and no unloading can occur.

3 | NUMERICAL EXAMPLES

All simulations have been performed in *FEAP*[44] using the displacement control. A cutting algorithm is implemented so that if convergence cannot be achieved after 20 iterations, the increment is repeated with half a size. The procedure is repeated until the increment size is small enough to converge, but if more than 10 cuts are necessary, the computation is aborted without reaching the desired value of the displacement. If after cutting an increment size, the convergence is achieved in 5 or less iterations, the original increment size is restored in the next increment. On the other hand, if 6 to 20 iterations are needed to converge after cutting the increment, the reduced converging increment size is kept until the required number of iterations to converge is 5 or less.

The advantages of using beam elements instead of solid elements in delamination simulations relate to a noticeable reduction in the overall degrees of freedom of the problem, and are discussed in detail in References 20 and 24. In this study, we further investigate the computational efficiency and accuracy of the quadratic linked interpolation compared to the standard linear Lagrange interpolation used in TB2 combined with BINT4 elements. For simplicity, we henceforth refer to the former model as (TB2+BINT4)Q and to the latter as (TB2+BINT4)L where "Q" and "L" stand for "quadratic" and "linear" (interpolation), respectively.

The numerical tests are set up in a way to provide an instructive assessment of the quadratic linked interpolation against the standard linear interpolation. To this end, the tests are divided in two groups, depending on the shear stiffness of the beam layers.

3.1 | Isotropic layers

In nonauxetic isotropic materials such as metals the shear modulus always takes the value between $E/3$ and $E/2$ and here we select from the literature five delamination tests with metal layers. For each test, material properties of the layers

and the interface are given in Table 1. In each test, the element size required to obtain an accurate and smooth solution is identified and compared between (TB2+BINT4)L and (TB2+BINT4)Q. Solution time, as well as the number of iterations and increment cuts are also compared to evaluate the numerical efficiency of the two possible types of the beam-interface coupling.

3.1.1 | Mode-I delamination examples

Two standard DCB tests[6,49] and a tapered double cantilever beam (TDCB) test are used for the mode-I analysis. The test configurations (Figure 3) consists of two equal plates (layers) mutually connected by means of an adhesive layer which

TABLE 1 Material properties of the specimens used in the selected delamination tests

	Layers		Interface		
Delamination test	***E* (GPa)**	***G* (GPa)**	**Ω (N/mm)**	**σ_{max} (MPa)**	**δ_0 (μm)**
DCB[45]	65.7	25.3	2.7	14	3.85
DCB[46]	114	42.85	2.846	36	13.09
TDCB[46]	72.4	27.21	2.846	36	13.09
ENF[47a]	150	60	1.45	80	0.008
MMB[48a]	71	26.7	1.65	52.5	6.65

[a]Same interface parameters are used in modes I and II.

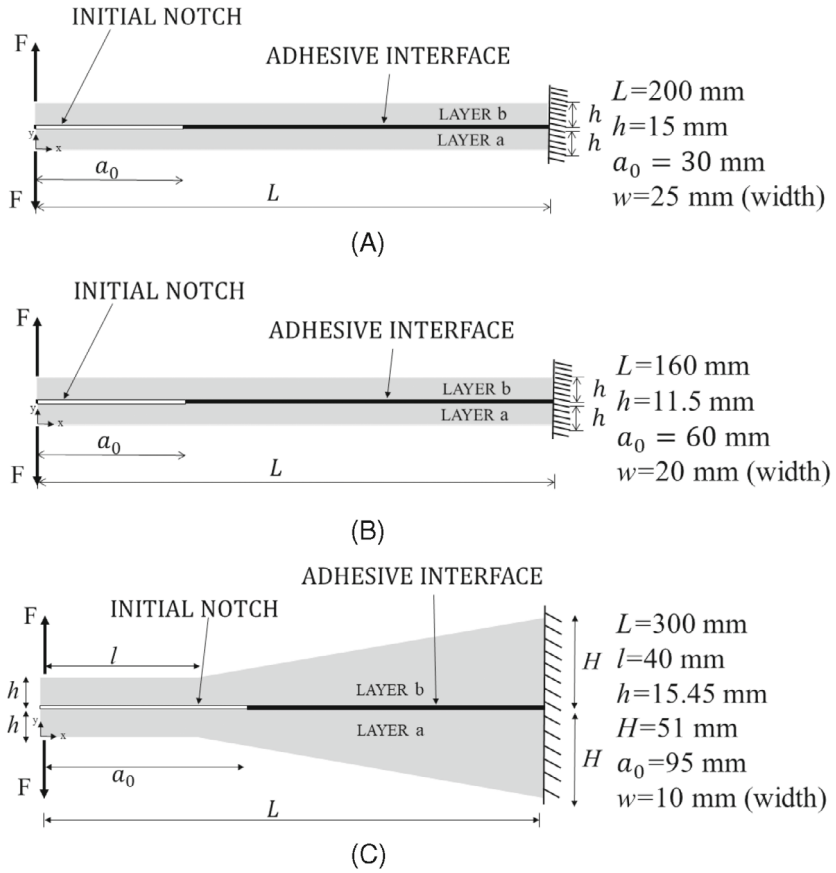

FIGURE 3 Configuration of mode-I tests with the corresponding geometrical properties for (A) DCB from Reference 45, (B) DCB from Reference 46, and (C) TDCB from Reference 46

are pulled apart by two transversal forces of opposite direction at the free end. In the deformed state, the layers will bend symmetrically with respect to the longitudinal axis passing through the middle of the interface. The two points (nodes) at the same co-ordinate x, but at different edges of the interface (e.g., nodes 1 and 4, or 2 and 3 in Figure 1), will have the same horizontal displacements ($u_1 = u_4$ and $u_2 = u_3$) and the same, but opposite vertical displacements ($v_1 = -v_4$ and $v_2 = -v_3$) in the deformed state. Thus, no relative displacement in mode II exists at the interface and, as a consequence, pure mode-I opening is obtained. This result is also obtained from Equation (1) because there is no horizontal displacement ($u_a = u_b = 0$) and, due to symmetry, we have $\theta_a = -\theta_b$ and $h_a = h_b$.

Because the mode-I tests are symmetric, it is convenient to model only one half of the problem. If we assume that only the upper arm of the structure is modeled, the top nodes of an interface element (nodes 4 and 3 according to Figure 1) will be attached to the arm, while the bottom nodes (nodes 1 and 2 according to Figure 1) should lay on the symmetry axis. However, prescribing boundary conditions at the symmetry axis that would reproduce the correct structural behavior of the full specimen (with two arms) is not straightforward. Because the nodes on the bottom edge of the layer will move not only vertically, but also horizontally, the nodes at the symmetry axis should have the same horizontal displacements, that is, no relative displacement in mode II should exist at the interface. Because this is not necessarily achieved even if the nodes at the symmetry axis are free to move horizontally, a correction in the constitutive law of the interface element is alternatively implemented by setting the stiffness in mode II equal to zero, that is, setting $k_{\mathrm{II}} = 0$ in Equation (6). It has been confirmed by our preliminary simulations that employing such a condition in the single-arm model, where the nodes at the symmetry axis are pinned (or clamped in the beam model), produces results that perfectly correspond to those of the full model with two arms. Moreover, the robustness of the single-arm model is greater than that of the full model. In needs to be emphasized that the right-hand end of the beam is modeled as clamped, which does not correspond to the actual test configuration,[6,49] but does not affect the results up to the very end of the test and is also in accordance with the examples presented in References 16 and 24.

Note that in the symmetric model, the values of the parameters in Table 1 must be adjusted. In particular, $\delta_{0.\mathrm{I}}$ and $\delta_{c.\mathrm{I}}$ are to be divided by two, while keeping the same $\sigma_{\max.\mathrm{I}}$, which then results in half the value of Ω_{I} and twice the value of k_{I} with respect to the full model.

In the first example,[45] it can be shown that if DCB problems are solved assuming negligible shear (i.e., using EB beam theory), as is the case in Reference 20, the peak force is overestimated and therefore employing TB elements is necessary for an accurate solution of the problem (see Figure 4). It can be noticed that the EB model overestimates the stiffness and the bearing capacity of the DCB before failure, which, from an engineering point of view, is not desirable. The analytical solutions proposed in Reference 29 are used for the EB and TB models which is equivalent to using a finite-element model (TB2+BINT4)Q or (TB2+BINT4)L with a sufficiently fine mesh, and are compared with those of the 2D-solid finite element results from Reference 50. Figure 4 clearly shows that the TB model is an efficient and accurate alternative to the 2D solid model which cannot be said for the EB model.

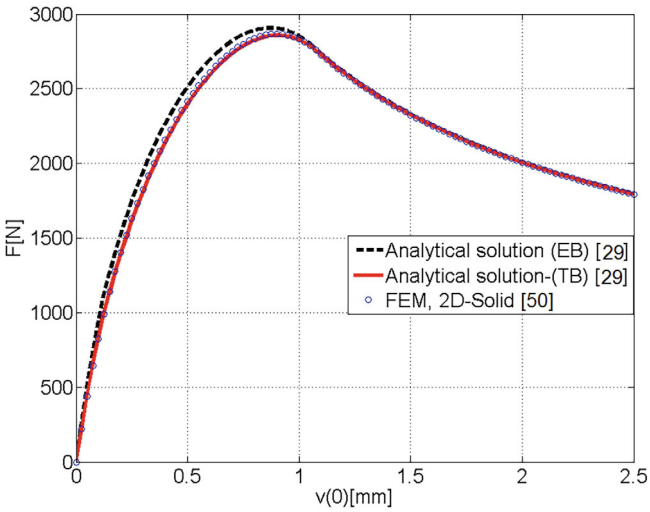

FIGURE 4 Comparison of the solutions based on Euler–Bernoulli and Timoshenko beam theory with those obtained using a 2D-solid model for the DCB test from Reference 45

TABLE 2 Comparison of solution summaries for (TB2+BINT4)L and (TB2+BINT4)Q models in mode-I tests

Test type	FE model	Element size (mm)	Iteration numbers	Computational time (s)
DCB[45]	(TB2+BINT4)L	10	219	0.09
	(TB2+BINT4)Q	10	239	0.1
DCB[46]	(TB2+BINT4)L	4	246	0.14
	(TB2+BINT4)Q	4	281	0.13
TDCB[46]	(TB2+BINT4)L	5	404	0.2
	(TB2+BINT4)Q	5	323	0.17

The summary of the solutions to mode-I tests is given in Table 2 which all are completed with no increment cuts. It can be seen that for a given element size, the computational cost is almost the same for both element types. However, based on the simulation results shown in Figures 5–7, it is clear that when using (TB2+BINT4)Q, an accurate and smooth solution, in contrast that obtained when using (TB2+BINT4)L, is always achieved. This implies that to obtain a comparable accuracy of the solution, with (TB2+BINT4)Q we may utilize coarser meshes, which saves computational time with respect to (TB2+BINT4)L. The size of the cohesive elements in our DCB examples (Figures 5B and 6B) is approximately 1/3 of the length of the cohesive zone, which is approximately 32 and 13.5 mm (calculated as in Reference 29), respectively. Typically, the size of the cohesive elements should be less than cca one-fifth to one-third of the cohesive-zone size[43] in order to obtain an accurate result. This comparison additionally confirms the high accuracy and efficiency of the proposed model.

3.1.2 | Mode-II delamination example

The ENF test is the standard test[7] for delamination in pure mode II. It is essentially a three-point bending test of an adhesively bonded two-layer beam with an initial notch at the left-hand side, as shown in Figure 8. Here the ENF test is used to compare the aforementioned (TB2+BINT4)Q and (TB2+BINT4)L models in mode II. Due to compression at the interface, no delamination in mode I can occur. On the other hand, due to shear tractions generated at the interface as the specimen bends, the crack will propagate toward the center of the specimen. Unlike the previous example, the ENF test is not symmetric and full specimen has been modeled with the boundary conditions given in Figure 8A. The input data for this test are given in Figure 8A and in Table 1.

A special type of BINT4 element is used at the initial notch in both models from F, such that no tractions, expect for the compression in mode I, can be transmitted between the layers. For such an element, it is sufficient to redefine $\boldsymbol{U}$ from Equation (33) as

$$\boldsymbol{U} = \begin{bmatrix} \frac{\langle -\delta_{\mathrm{I}} \rangle}{|\delta_{\mathrm{I}}|} k_{\mathrm{I}} & 0 \\ 0 & 0 \end{bmatrix}, \tag{37}$$

with its U_{11} component nonzero only if $\delta_{\mathrm{I}} < 0$. Using definition (37), $\boldsymbol{\sigma}$ is expressed as $\boldsymbol{\sigma} = \boldsymbol{U}\,\boldsymbol{\delta}$ throughout the analysis, while the vector of residual forces and the stiffness matrix of the notch interface element then follow from Equations (25) and (36).

The results of simulations with an element size of 0.3125 mm are shown in Figure 9, where it can be noticed that the results of the models (TB2+BINT4)Q and (TB2+BINT4)L overlap. In addition, 523 iterations, and 18 increment cuts take place in both models. This is because, as it can be seen in Equation (1), only delamination in mode I is affected by the quadratic term used for the interpolation of the transversal displacements in (TB2+BINT4)Q model. It can be therefore concluded that, in contrast to pure mode I, in pure mode II (TB2+BINT4)Q is equivalent to (TB2+BINT4)L. In addition, the result of a 3D FEM[47] is added in Figure 9 for the sake of comparison.

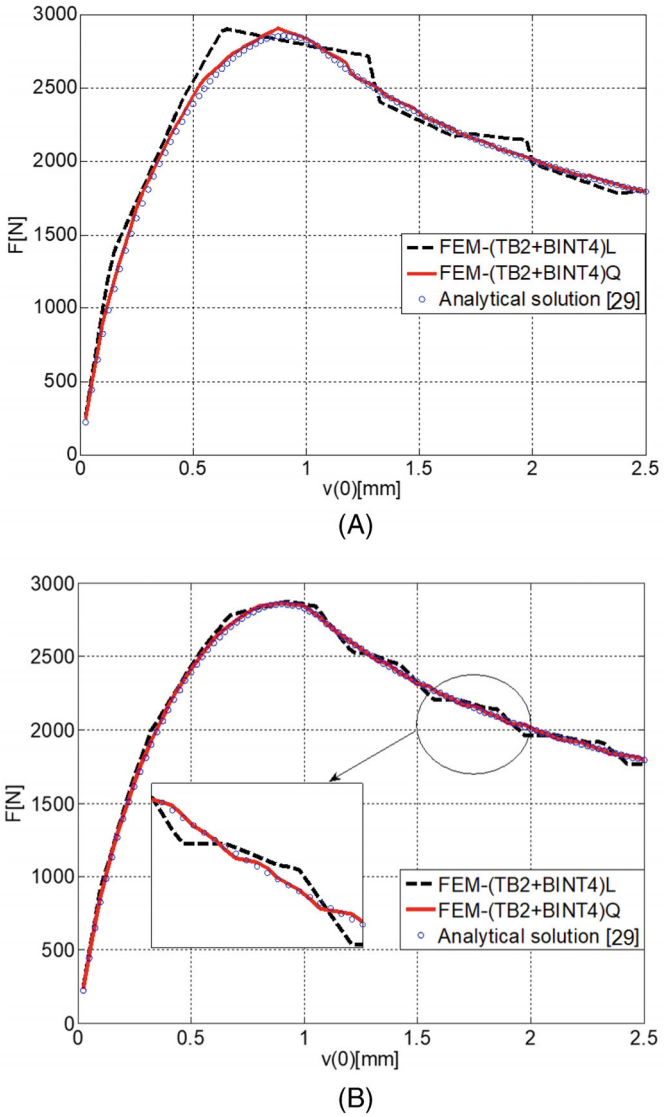

FIGURE 5 Comparison of the performance of (TB2+BINT4)L and (TB2+BINT4)Q models in the DCB test from Reference 45 for (A) $L_e = 20$ mm and (B) $L_e = 10$ mm

3.1.3 | Mixed-mode delamination example

The standard mixed-mode bending (MMB) test[8] is employed to assess the performance of the (TB2+BINT4)Q against (TB2+BINT4)L in mixed-mode conditions. This test is essentially an extension of the ENF test, where, in addition to the downward force at the midspan, an upward force that opens the interface in mode I is added at the left-hand side of the upper layer (see Figure 8B). In this way, a combination of delaminations in modes I and II is obtained, and the relative contribution of each of the modes can be changed by adjusting the length of the rigid lever c in Figure 8B.

The simulation results and solution summary are given in Figure 10 and Table 3, respectively. It can be seen that, as in the mode-I tests, in the mixed-mode test (TB2+BINT4)Q provides much faster convergence than (TB2+BINT4)L for the same mesh, which can save a significant amount of computational time (see the last column in Table 3).

From all the presented results for problems with metal layers, it can be concluded that (TB2+BINT4)Q model can provide more accurate solutions and improve the convergence for the same mesh size in mode-I and mixed-mode delamination tests compared to (TB2+BINT4)L. On the other hand, such a modification of interpolation functions does not affect the results in pure mode-II (ENF) test. This is an expected result, since adding the quadratic term in the interpolation of vertical displacements of the 2-node TB element only alters the interpolation function for the normal separation, while the interpolation function for tangential separation remains unaltered (see Equations 18 and 19).

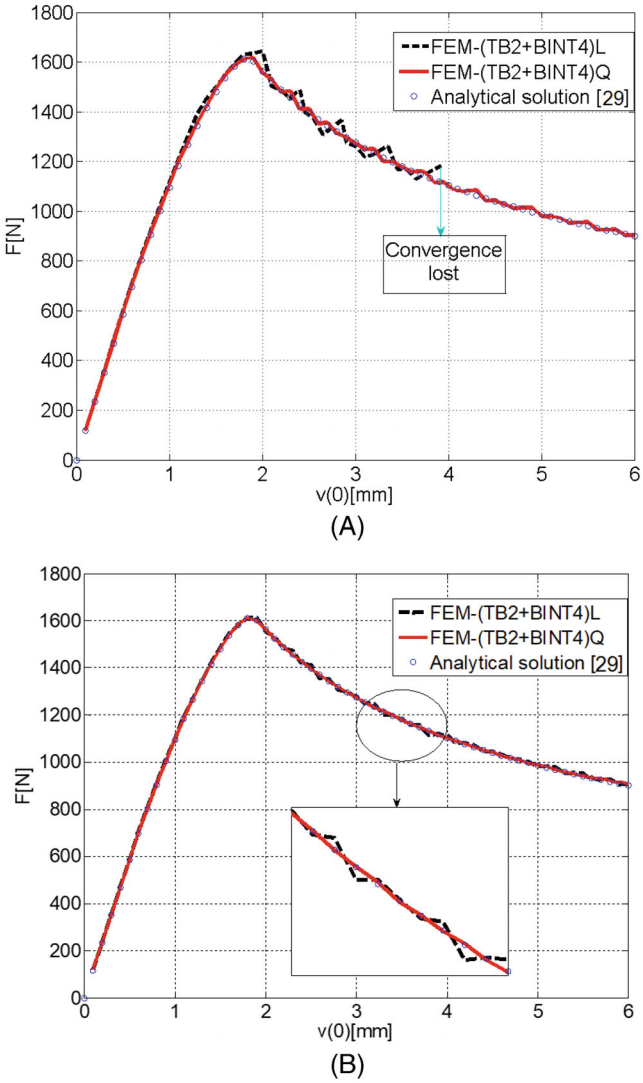

FIGURE 6 Comparison of the performance of (TB2+BINT4)L and (TB2+BINT4)Q models in the DCB test from Reference 46 for (A) $L_e = 8$ mm and (B) $L_e = 4$ mm

3.2 | Orthotropic layers with stiff interface

In all examples from the previous section, metal layers have been used. However, delamination often occurs in laminated composites (such as carbon-fiber reinforced polymers—CFRP[16,24]), where two important differences take place. First, the bulk material is orthotropic with shear modulus relatively low compared to Young's modulus. In such a case, shear and Young's moduli cannot be related via $E/3 < G < E/2$ as before. Ignoring shear deformability in such cases (by using EB beam theory) could thus introduce non-negligible errors in the analysis. Secondly, the adhesives used in composites often have a very high stiffness in the linear-elastic range,[16,19,26] which is defined by parameters k_{I} and k_{II} in Equation (6). This means that at the interface, relatively high tractions can be transmitted between the layers, while the relative displacement (opening) is extremely small. In addition, they can be very brittle, which means that they have a relatively low δ_c.

As it will be shown below, in situations where the layers have a relatively low value of the shear modulus and the interface is stiff, shear strains significantly influence the deformed shape of the elements' reference axes when the quadratic linked interpolation is employed. In turn, the (TB2+BINT4)Q model actually loses its advantages over (TB2+BINT4)L and in certain important delamination scenarios behaves quite poorly. To investigate this, the example presented in Reference 51 is used. Geometrical and material properties of the layers and interface are summarized in Table 4, where the material properties of the interface are the same in modes I and II. Note that $G \approx E/26$, while $k_i = \sigma_{\max.i}/\delta_{0.i} =$

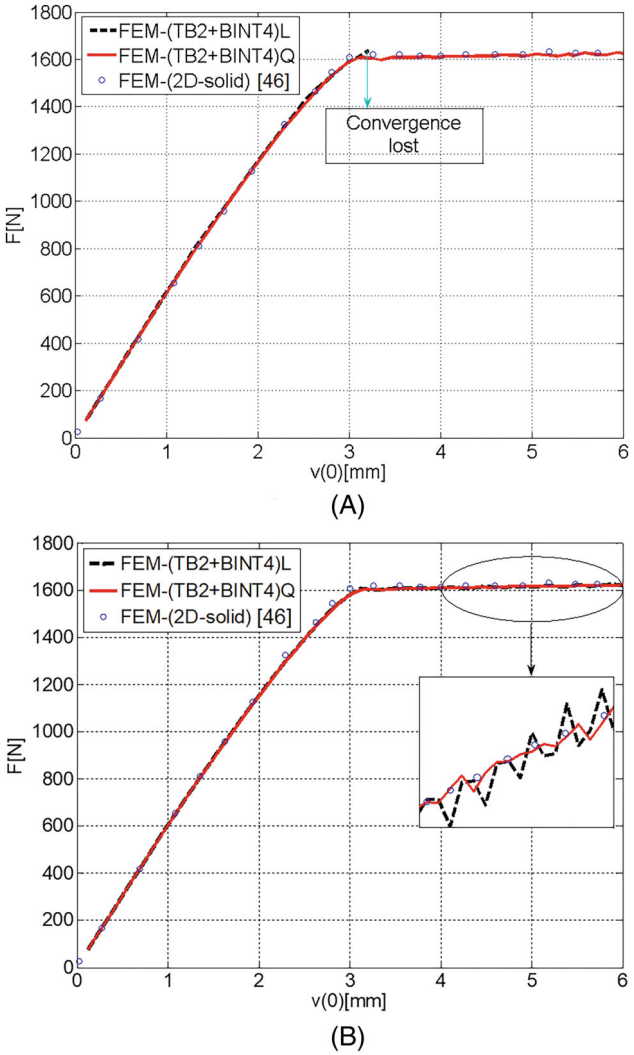

FIGURE 7 Comparison of the performance of (TB2+BINT4)L and (TB2+BINT4)Q models in the TDCB test from Reference 46 for (A) $L_e = 10.25$ mm and (B) $L_e = 5$ mm

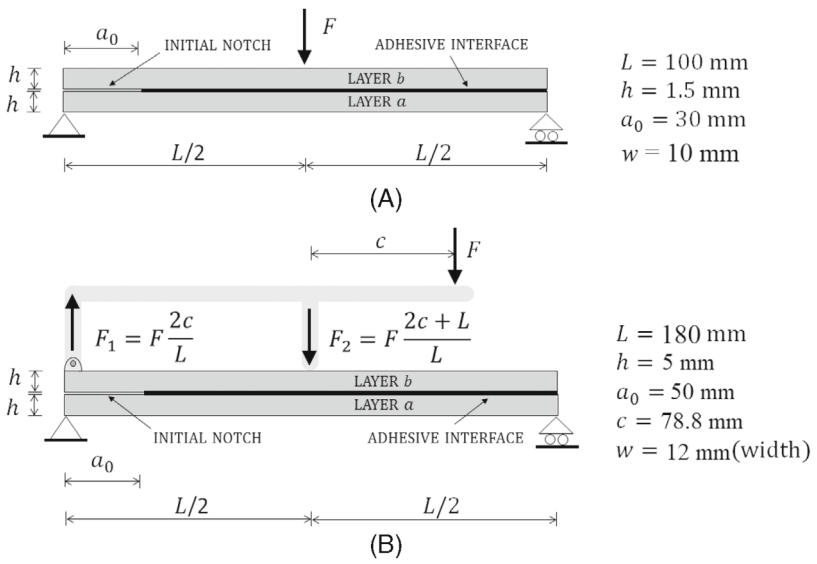

FIGURE 8 Configuration of the (A) ENF test from Reference 47 and (B) MMB test from Reference 48, with the corresponding geometrical properties

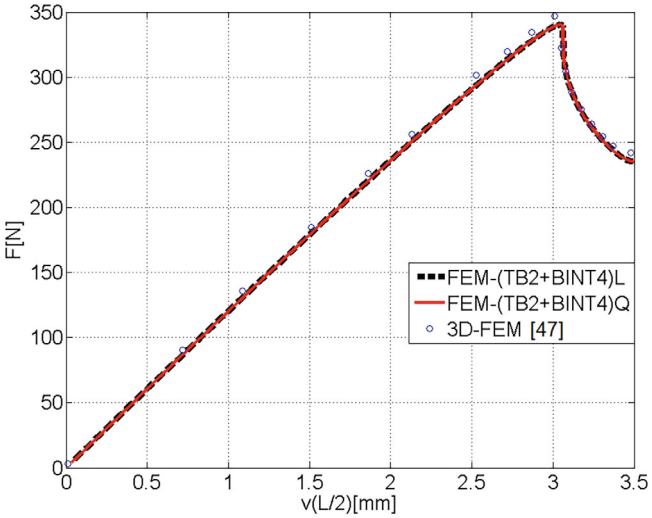

FIGURE 9 Comparison of the performance of (TB2+BINT4)Q and (TB2+BINT4)L models in the ENF test from Reference 47

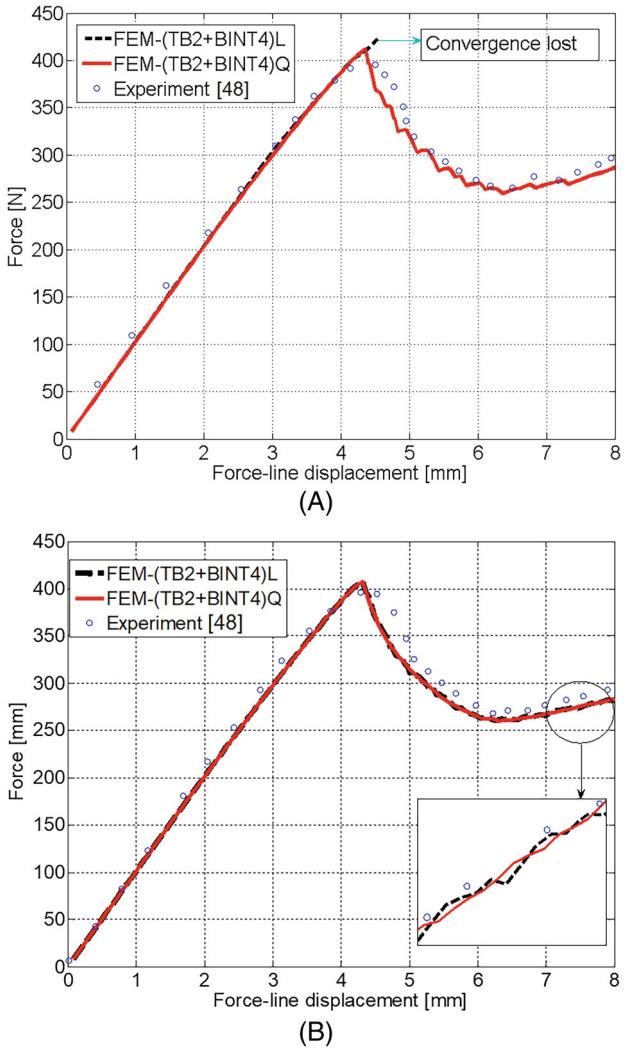

FIGURE 10 Comparison of the performance of (TB2+BINT4)L with (TB2+BINT4)Q models in the MMB test from Reference 48 for (A) $L_e = 5$ mm and (B) $L_e = 2$ mm

TABLE 3 Comparison of solution summaries for (TB2+BINT4)L and (TB2+BINT4)Q model in the mixed-mode test[48] for the finite-element mesh with $L_e = 1$ mm

Element type	Iteration numbers	Increment cuts	Computational time (s)
(TB2+BINT4)L	642	8	13.02
(TB2+BINT4)Q	400	1	8.56

TABLE 4 Geometrical and material specification of the composite delamination test

Geometrical specifications (mm)	$L = 100$	$h = 1.5$	$a_0 = 30$	$w = 1$	$c = 41.5$
Material specifications	$E = 135$ GPa	$G = 5.2$ GPa	$\Omega = 4$ N/mm	$\sigma_0 = 57$ MPa	$\delta_0 = 0.1$ μm

$5.7 \cdot 10^8$ N/mm^3 (i =I, II), which confirms that in this example the shear modulus is low and the interface is stiff. DCB, ENF and MMB tests are simulated and the results provided by the models (TB2+BINT4)Q and (TB2+BINT4)L are compared.

3.2.1 | Mode-I delamination

In Figure 11A, the simulation of the DCB test with element size of 0.5 mm is presented. The simulation procedure terminates quickly with a loss of convergence for (TB2+BINT4)Q model, but not for (TB2+BINT4)L. To understand why this happens, let us look into the stress distribution along the interface for the two models during the final step for which (TB2+BINT4)Q still converges, shown in Figure 11B. While for (TB2+BINT4)L, a relatively smooth and accurate stress distribution is obtained, for (TB2+BINT4)Q spurious oscillations of very large amplitudes around the exact solution are observed.

The reason for such a behavior can be explained by looking at Figure 12 where the normal separation δ_{I} between reference axes of two adjacent interface elements is shown in the deformed configuration. Note that because $\delta_{\mathrm{I}} = 2v_b = -2v_a$, this plot qualitatively also represents the shape of the deformed reference axis of the upper layer. The parabolic (quadratic) shape is clearly visible with a first-derivative (slope) discontinuity at the common node (at $x = 31.5$ mm). This discontinuity is known to exist in TB finite elements because at the boundaries of each element the continuity is enforced only for the cross-sectional rotations, which are different from the slope of the reference axis, as discussed at the end of Section 2.1. In this particular example, the interface is very stiff, which results in relatively small transversal displacements at the interface. Note that this does not mean that the slope of the reference axis is also very small, because, as it can be easily demonstrated by taking the derivative with respect to x of Equation (15), v' depends not only on the nodal transversal displacements, but also on the nodal cross-sectional rotations.

In addition, because for the orthotropic material in this example the shear modulus is relatively low with respect to Young's modulus, the layers are highly shear-deformable, which results in a significant deviation of the right angle between the plane of the cross section and the reference axis. According to Equation (26), this means that a significant part of the cross sectional rotation θ is due to shear strains γ. Thus, in this example we have very small transversal displacements with relatively high cross-sectional rotations of layers. From Equation (15), it then follows that the quadratic (parabolic) part of the interpolation (third term) is dominant with respect to the linear part (first two terms). This explains the shape of the distribution of normal separation in Figure 12.

When this parabolic shape of the reference axis is transferred to the interface, it results in tensile stresses at the edges of the element and compressive stresses in the middle, as also shown in Figure 12 (secondary vertical axis). It can be seen that this pattern is repetitive along the interface and, as visible in Figure 11B, it is most pronounced close to the crack tip (where the shear forces in the layers reach their maximum values) and vanishes as we move away from it. Note that tensile stresses do not go beyond $\sigma_{\max,\mathrm{I}}$, while in compression the stresses are unlimited (because in the CZM used no damage can occur in compression) and follow the linear-elastic constitutive law given in Equation (5). In fact, in Figure 12 it can be noticed that in all integration points that have positive values of separation (except the one at $x = 31.375$ mm), $\delta_{\mathrm{I}} > \delta_{0,\mathrm{I}}$ (where $\delta_{0,\mathrm{I}} = 10^{-7}$ mm), which means that the interface is damaged. However, due to the fact that the softening branch in this example is much longer than the linear-elastic branch ($\delta_{c,\mathrm{I}} = 0.14$ mm), this damage is very small and the resulting stresses are very close to $\sigma_{\max,\mathrm{I}}$.

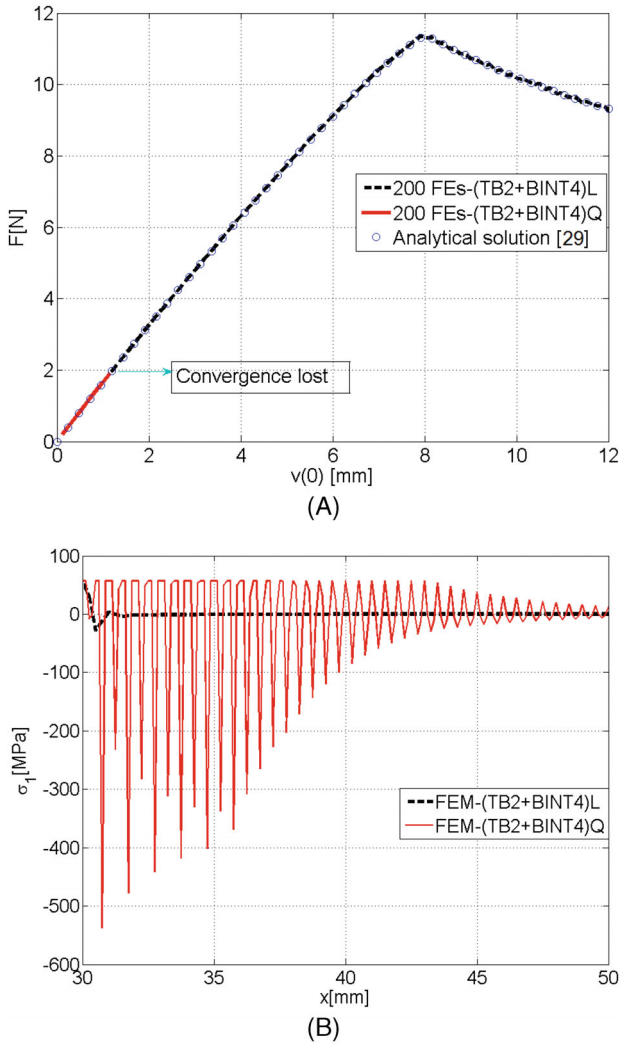

FIGURE 11 Comparison between (TB2+BINT4)Q and (TB2+BINT4)L in a DCB test with composite layers and a stiff interface: (A) Load-displacement plot and (B) mode-I stress distribution along the interface

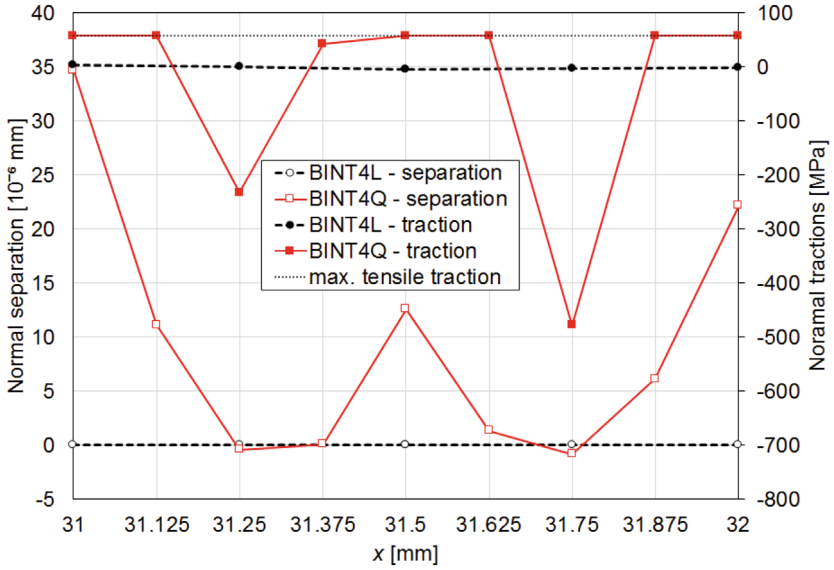

FIGURE 12 Normal separation and normal traction (on the secondary vertical axis) in integration points of two adjacent BINT4L and BINT4Q interface elements for the DCB example with orthotropic layers and a stiff interface

On the other hand, in Figure 11B no repetitive oscillations of interface tractions can be noticed for the model with standard linear Timoshenko elements. This is so because in that case the cross-sectional rotations (that are also increased due to a significant amount of shear strains) do not affect the distribution of transversal displacements within an element. In turn, this will result in smaller values of the normal separation and normal tractions at the interface compared to the case with quadratic linked interpolation, which is clearly visible from Figure 12. We can also see that the distribution of tractions at the interface with linear elements is much smoother and clearly resembles the well-known distribution where behind the crack tip, a relatively small part of tensile tractions is followed by compressive tractions that asymptotically approach zero away from the crack tip. However, tractions in linear interface elements can oscillate if the finite-element mesh is not sufficiently fine. In this example this happened at $x = 31$ mm, where normal traction is positive, while in two surrounding integration points compressive tractions are obtained. As it can be seen in Figure 11A, this imprecision still allows the solution procedure to converge and, although numerically induced oscillations are present on the part where the crack is propagating, full force-displacement curve is obtained.

It turns out that the quadratic term, which has been shown to be beneficial in mode-I examples presented in Section 3.1.1 becomes detrimental in the present one. This is because in those examples the stiffness of the interface was approximately 200 times less and the shear-to-bending-stiffness ratio approximately 10 times higher compared to this example. A simple parametric analysis shown in Figure 13 confirms that by reducing the stiffness of the interface and increasing the shear modulus of the DCB arms the performance of the model with quadratic linked interpolation is significantly improved. For the sake of simplicity, a linear-elastic constitutive law of the interface is assumed, which means that the crack is not allowed to propagate. Thus, the aim is not to analyze the convergence during the crack propagation phase, but to compare the accuracy of the numerical models based on TB elements with either linear or linked quadratic interpolation with respect to the exact (analytical) solution.

A comparison of the normal separation at the interface (analogous to that presented in Figure 12) is now given in Figure 13 for different values of the stiffness of the interface and shear modulus of the arms. Case A corresponds to the parameters given in Table 4, so that $k_A = 5.7 \cdot 10^5$ N/mm^3 and $G_A = 5.7$ GPa. For Case B, the stiffness of the interface is reduced 10 times ($k_B = k_A/10$, $G_B = G_A$), while for Case C, the shear modulus is increased 10 times ($k_C = k_A$, $G_C = 10G_A$).

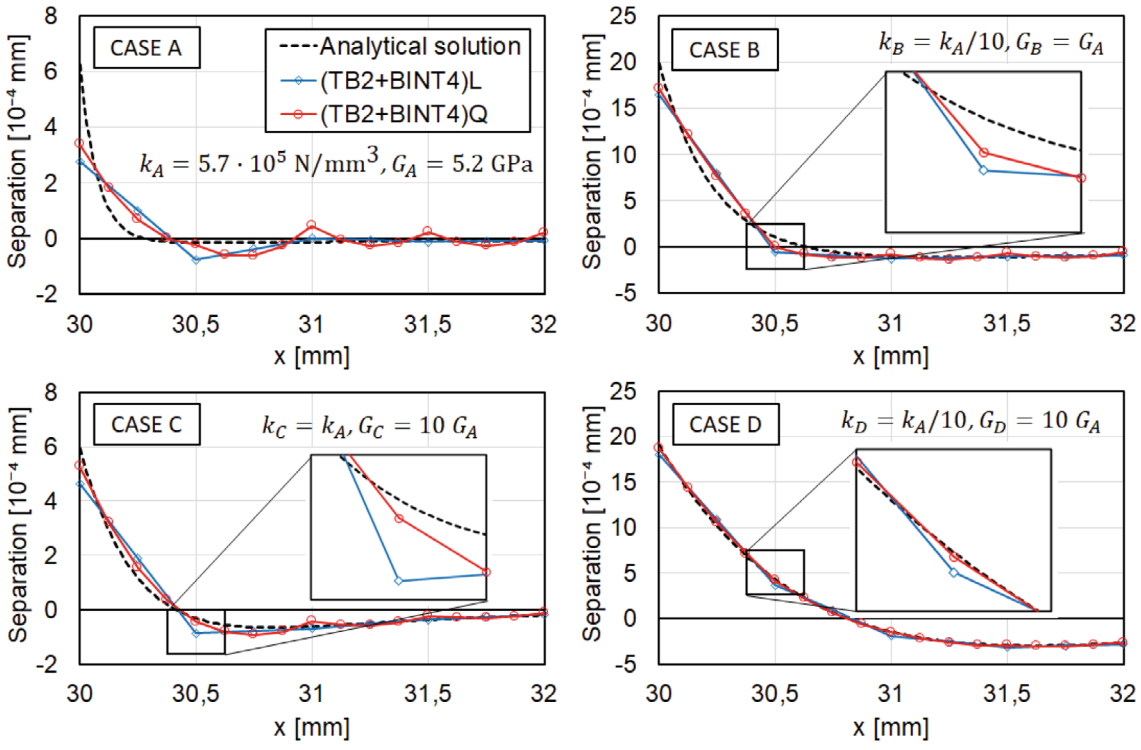

FIGURE 13 A comparison of the normal separation at the interface obtained by the numerical models based on Timoshenko beam elements with either linear ((TB2+BINT4)L) or linked quadratic interpolation ((TB2+BINT4)Q) with respect to the analytical solution for four cases of material parameters k (stiffness of the interface) and G (shear modulus of the arms)

Case D is a combination of Cases B and C, that is, $k_D = k_A/10$ and $G_D = 10G_A$. Only the first 2 mm of the interface corresponding to 4 elements of size $L_e = 0.5$ mm are shown in Figure 12. The results are obtained for the applied load equal to 2 N, which corresponds to the point in Figure 11A where (TB2+BINT4)Q lost convergence.

Except for Case A, results of the model with linked quadratic interpolation (TB2+BINT4)Q are closer to the exact (analytical) solution, which has been derived in Reference 29. As expected, the agreement of both (TB2+BINT4)L and (TB2+BINT4)Q with respect to the analytical solution is the best for Case D. For all cases (TB2+BINT4)Q gives a more accurate crack-tip displacement than (TB2+BINT4)L. It has to be emphasized that by increasing the shear modulus 10 times, shear-to-bending stiffness in this example becomes comparable to those from mode-I examples in Section 3.1.1, which corresponds to an isotropic material with Poisson's ratio equal to 1/3. On the other hand, even after reducing it 10 times, the stiffness of the interface in this example is still approximately 20 times higher than those from mode-I examples in Section 3.1.1.

The main advantage of the formulation with the linked quadratic interpolation can be seen when the length of the elements is increased, which is shown in Figure 14 for $L_e = 1$ mm and $L_e = 2$ mm. Unlike (TB2+BINT4)L, (TB2+BINT4)Q maintains a relatively high accuracy even after the number of finite elements is reduced 4 times. This property is the biggest advantage of the proposed FE formulation because it allows to obtain accurate (smooth) solutions for delamination problems with relatively coarse meshes, as demonstrated in Section 3.1.1.

It can be concluded that when the contribution of the quadratic term in Equation (15) with respect to the linear terms is reduced, its effect (a curved reference axis of the beam) is obviously beneficial in the zone of the interface close to the crack tip. The easiest way to avoid convergence problems in examples with relatively stiff interface and shear-deformable arms is simply to exclude the quadratic term in Equation (15) and essentially convert the (TB2+BINT4)Q model to (TB2+BINT4)L. A novel TB finite element that would additionally allow also for continuity of the first derivative of the vertical displacement (i.e., the slope of the reference axis) would likely eliminate this problem. This will be discussed in more detail in Section 4 as an idea for the future research.

3.2.2 | Mode-II delamination

The peculiar behavior encountered in mode I and discussed above, does not occur in mode II. As explained earlier, the contribution of the quadratic linked interpolation in pure mode-II delamination vanishes. This can be seen in Figure 15 where perfect agreement both in the load-displacement curve and in the distribution of the tangential tractions at the interface can be noticed.

3.2.3 | Mixed-mode delamination

When modes I and II are combined in the MMB test, the results of (TB2+BINT4)Q model are again very poor (see Figure 16A). In Figure 16B,C, it can be noticed that in the (TB2+BINT4)Q model both the normal and tangential stresses

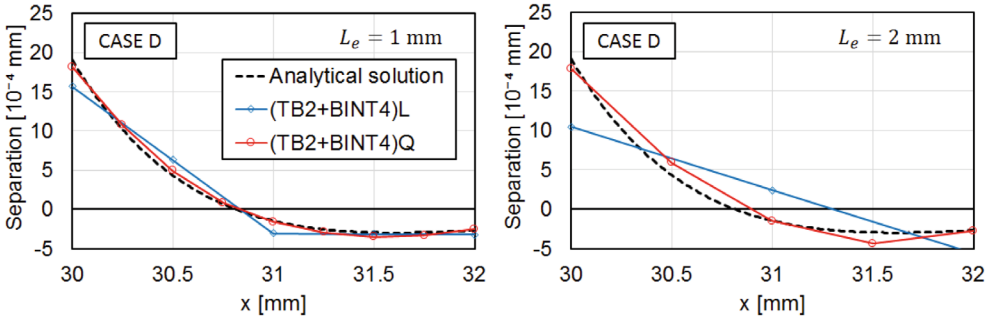

FIGURE 14 A comparison of the normal separation at the interface obtained by the numerical models based on Timoshenko beam elements with either linear ((TB2+BINT4)L) or linked quadratic interpolation ((TB2+BINT4)Q) with respect to the analytical solution for length of the element $L_e = 1$ mm and $L_e = 2$ mm

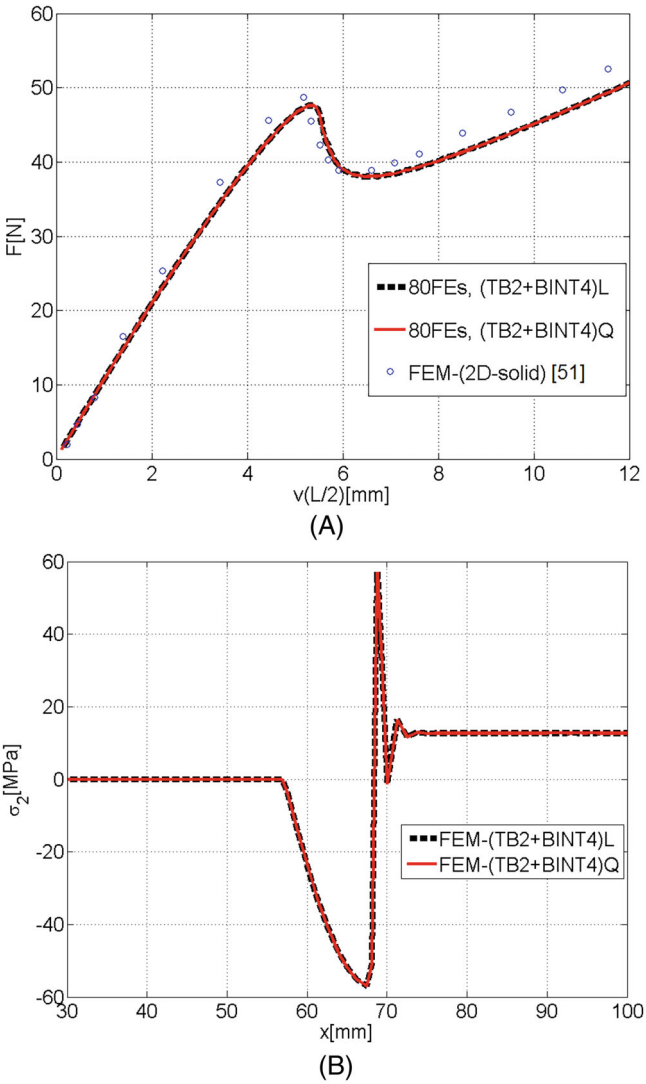

FIGURE 15 Comparison between (TB2+BINT4)Q and (TB2+BINT4)L in a ENF test with composite layers and a stiff interface: (A) Load-displacement plot and (B) mode-II stress distribution along the interface

at the interface oscillate. At first, this might seem strange because we have previously seen that the quadratic linked interpolation does not affect the pure mode II. However, in mixed-mode delamination, as shown in Equation (4), the normal and tangential relative displacements are coupled in the damage variable and the spurious oscillations in the normal direction are consequently transferred to the tangential direction (see Figure 16C). As for the DCB test, removing the quadratic term in Equation (15) solves the problem by converting (TB2+BINT4)Q to (TB2+BINT4)L. As shown in Figure 16A, the latter can indeed simulate the whole test.

4 | CONCLUSION AND OUTLOOK

In this work, the use of two-node TB finite elements with quadratic linked interpolation for modeling mixed-mode delamination is studied. In the proposed model, the interpolation function of transversal displacements is composed of a linear term involving nodal transversal displacements and a quadratic term involving nodal cross-sectional rotations (see Equation 15). The fields of axial displacements and cross-sectional rotations are interpolated using linear Lagrange polynomials. The formulation of the so-called beam-linked 4-node interface element that, unlike the standard interface element used in conjunction with 2D solid finite elements, is compatible with degrees of freedom of beam finite elements, is also presented. The formulation is general and it can be easily adopted to different shapes of TSLs and different

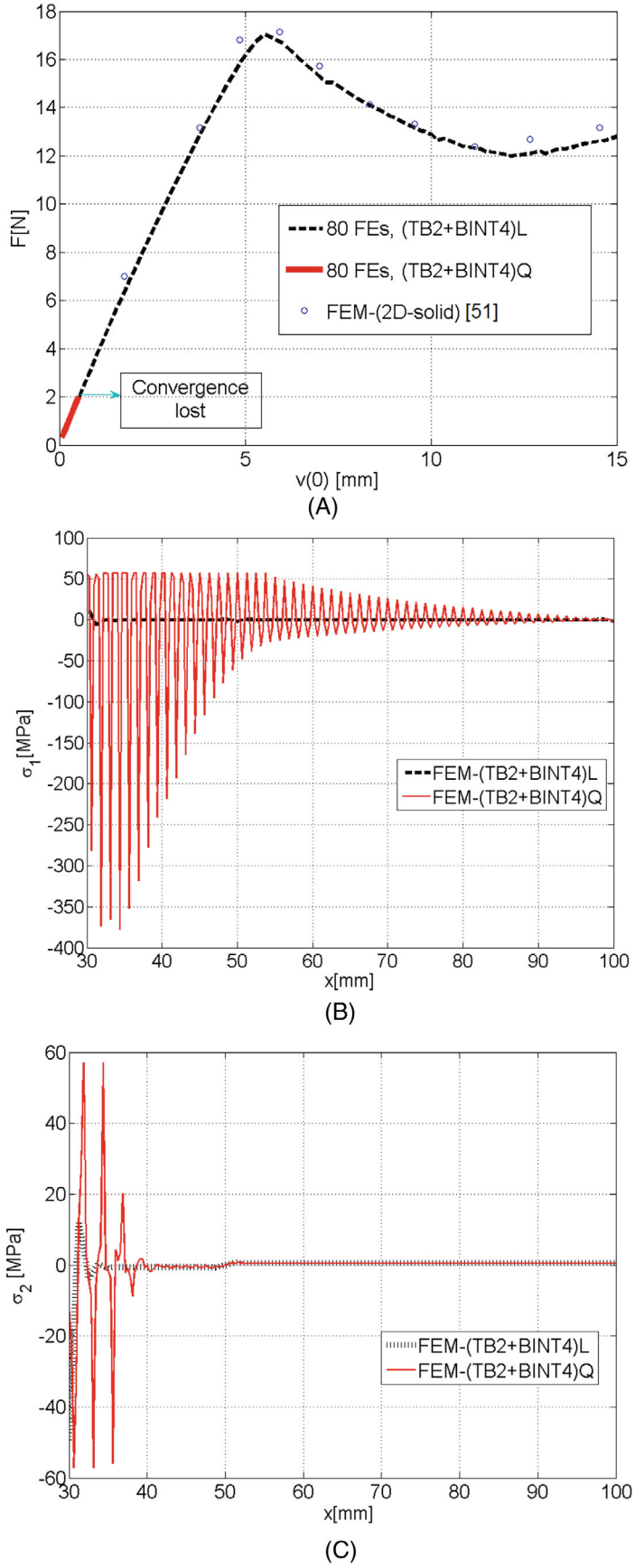

FIGURE 16 Comparison between (TB2+BINT4)Q and (TB2+BINT4)L in a MMB test with composite layers and a stiff interface: (A) Load-displacement plot and stress distribution along the interface in (B) mode I and (C) mode II

interpolation functions. In fact, interface elements must inherit the interpolation functions from the adjacent beam finite elements.

A comparison of a FEM with linear interpolation functions, denoted as (TB2-BINT4)L, and an analogous model with quadratic linked interpolation functions, denoted as (TB2-BINT4)Q, is performed on several mode-I, mode-II and mixed-mode delamination examples from the literature. It has been demonstrated that the approach with quadratic linked interpolation for the same mesh gives the converged results that are closer to the reference solutions in mode I. Therefore, in order to obtain results of satisfactory accuracy, a coarser mesh can be used, which in turn results in reduction of the computational time.

On the other hand, changing from linear to quadratic linked interpolation has no influence on the behavior in pure mode II. This is because, as it can be seen from Equation (1), the transversal displacements of adjacent layers (and therefore their interpolation functions), have no influence on the relative displacements in mode II. When modes I and II are coupled, the aforementioned advantages of (TB2-BINT4)Q formulation in mode I are transferred to the mixed-mode delamination problems.

However, it has been shown that the performance of the model with quadratic linked interpolation is dependent on the material properties of the layers and interface used in simulations. In particular, (TB2-BINT4)Q performs better for metal joints than for multi-layered composites with relatively stiff adhesives. For the latter, the layers have relatively low shear stiffness, while the interface is very stiff. In such conditions, relative displacements at the interface are very small and the layers' cross-sectional rotations become relatively large due to high shear strains present in the composite layers of low shear stiffness. As a consequence, the quadratic term in Equation (15) becomes dominant with respect to the linear one, which for a mode-I problem leads to a very pronounced C-1 discontinuity of the beam's axis at the nodes and spurious oscillations of the interface tractions. Such numerical anomalies become a major problem in obtaining a robust solution and (TB2-BINT4)Q model loses convergence at a very early stage (before the onset of delamination). While these problems do not appear in pure mode II (for the same reasons as explained before), in the mixed-mode problems, the spurious oscillations in mode I are transferred also to mode II through the coupling of the damage variable, which eventually leads to very poor results.

Such problems can be efficiently avoided by switching to the standard linear interpolation, which is something that can be easily done in the proposed formulation by canceling the quadratic term in Equation (15). It is possible to derive a formulation that would switch from (TB2-BINT4)Q to (TB2-BINT4)L when shear-related problems are encountered. However, the future work of this research group will be devoted to deriving and implementing a two-node TB element with C-1 continuity in the displacement field. Thus, besides the two components of displacement and a cross-sectional rotation, the first derivative of the transversal displacement (i.e., the slope of the axis of the beam) should be added as an additional degree of freedom in each node. Although in such an approach additional degrees of freedom are introduced, it is expected that the computational time will not be increased because the model will be more accurate and robust, therefore allowing for coarser meshes to be used in order to obtain accurate results.

The presented finite-element formulation represents a framework for further development of beam-based finite-element formulations with enhanced interpolation functions, as well as different types and shapes of CZMs suitable for dynamic and geometrically nonlinear analysis, where computational speed and robustness become increasingly important.

ACKNOWLEDGMENTS

The authors would like to acknowledge the Croatian Science Foundation (research projects IP-2016-06-4775 ASDEL and IP-2018-01-1732 FIMCOS) for their financial support and additional support by the University of Rijeka (research grant uniri-tehnic-18-248 1415). This project has also received funding from the European Union's Horizon 2020 research and innovation programme under the Marie Skłodowska-Curie grant agreement No 860124. This publication reflects only the author's view and the Research Executive Agency is not responsible for any use that may be made of the information it contains.

DATA AVAILABILITY STATEMENT

Data sharing is not applicable to this article as no datasets were generated or analyzed during the current study.

ORCID

Maedeh Ranjbar https://orcid.org/0000-0002-7433-253X

Leo Škec https://orcid.org/0000-0002-0074-7169
Gordan Jelenić https://orcid.org/0000-0001-5130-1223
Dragan Ribarić https://orcid.org/0000-0003-4810-5621

REFERENCES

1. Girhammar UA, Gopu VKA. Composite beam-columns with interlayer slip-exact analysis. *J Struct Eng*. 1993;119(4):1265-1282.
2. Seracino R, Oehlers DJ, Yeo MF. Partial-interaction flexural stresses in composite steel and concrete bridge beams. *Eng Struct*. 2001;23(9):1186-1193.
3. EN 1995-1-1. Eurocode 5: design of timber structures - Part 1-1: general - common rules and rules for buildings. Technical report, European Committee for Standardization (CEN); 2004.
4. Griffith AA. The phenomena of rupture and flow in solids. *Philos Trans Royal Soc Lond A*. 1921;221:163-198.
5. Irwin GR. Onset of fast crack propagation in high strength steel and aluminum alloys. Sagamore Research Conference Proceedings; Vol. 2, 1956:289-305.
6. ASTM D3433-99(2020). Standard Test Method for Fracture Strength in Cleavage of Adhesives in Bonded Metal Joints. Technical report, ASTM International, Pennsylvania; 2020.
7. ASTM D7905/D7905M – 14. Standard test method for determination of the mode II interlaminar fracture toughness of unidirectional fiber-reinforced polymer matrix composites. Technical report, ASTM International, Pennsylvania; 2014.
8. ASTM D 6671/D 6671M – 06. Standard Test Method for Mixed Mode I-Mode II Interlaminar Fracture Toughness of Unidirectional Fiber Reinforced Polymer Matrix Composites. Technical report, ASTM International, Pennsylvania; 2007.
9. Anderson TL. *Fracture Mechanics - Fundamentals and Applications*. 4th ed. CRC Press; 2017.
10. Dugdale DS. Yielding in steel sheets containing slits. *J Mech Phys Solids*. 1960;8:100-104.
11. Barenblatt GI. The mathematical theory of equilibrium cracks in brittle fracture. *Adv Appl Mech*. 1962;7:55-129.
12. Hillerborg A, Modéer M, Petersson PE. Analysis of crack formation and crack growth in concrete by means of fracture mechanics and finite elements. *Cem Concr Res*. 1976;6(6):773-781.
13. Hellweg HB, Crisfield MA. A new arc-length method for handling sharp snap-backs. *Comput Struct*. 1998;66(5):704-709.
14. Alfano G, Crisfield MA. Solution strategies for the delamination analysis based on a combination of local-control arc-length and line searches. *Int J Numer Methods Eng*. 2003;58(7):999-1048.
15. Škec L, Jelenić G. Geometrically non-linear multi-layer beam with interconnection allowing for mixed-mode delamination. *Eng Fract Mech*. 2017;169:1-17.
16. Alfano G, Crisfield MA. Finite element interface models for the delamination analysis of laminated composites: mechanical and computational issues. *Int J Numer Methods Eng*. 2001;50(7):1701-1736.
17. Turon A, Dávila CG, Camanho PP, Costa J. An engineering solution for mesh size effects in the simulation of delamination using cohesive zone models. *Eng Fract Mech*. 2007;74(10):1665-1682.
18. Bak BLV, Lindgaard E, Lund E. Analysis of the integration of cohesive elements in regard to utilization of coarse mesh in laminated composite materials. *Int J Numer Methods Eng*. 2014;99(8):566-586.
19. Lindgaard E, Bak BLV, Glud JA, Sjølund J, Christensen ET. A user programmed cohesive zone finite element for ANSYS mechanical. *Eng Fract Mech*. 2017;180:229-239.
20. Russo R, Chen B. Overcoming the cohesive zone limit in composites delamination: modeling with slender structural elements and higher-order adaptive integration. *Int J Numer Methods Eng*. 2020;121(24):5511-5545.
21. Crisfield MA, Alfano G. Adaptive hierarchical enrichment for delamination fracture using a decohesive zone model. *Int J Numer Methods Eng*. 2002;54(9):1369-1390.
22. Guiamatsia I, Ankersen JK, Davies GAO, Iannucci L. Decohesion finite element with enriched basis functions for delamination. *Compos Sci Technol*. 2009;69(15):2616-2624.
23. Sauer RA. Enriched contact finite elements for stable peeling computations. *Int J Numer Methods Eng*. 2011;87(6):593-616.
24. Škec L, Jelenić G, Lustig N. Mixed-mode delamination in 2D layered beam finite elements. *Int J Numer Methods Eng*. 2015;104(8):767-788.
25. Dávila CG, Camanho PP, Turon A. Effective simulation of delamination in aeronautical structures using shells and cohesive elements. *J Aircr*. 2008;45(2):663-672.
26. Bruno D, Greco F, Lonetti P. Computation of energy release rate and mode separation in delaminated composite plates by using plate and interface variables. *Mech Adv Mater Struct*. 2005;12(4):285-304.
27. Camanho PP, Davila CG, de Moura MF. Numerical simulation of mixed-mode progressive delamination in composite materials. *J Compos Mater*. 2003;37(16):1415-1438.
28. Yang QD, Fang XJ, Shi JX, Lua J. An improved cohesive element for shell delamination analyses. *Int J Numer Methods Eng*. 2010;83(5):611-641.
29. Škec L, Alfano G, Jelenić G. Complete analytical solutions for double cantilever beam specimens with bi-linear quasi-brittle and brittle interfaces. *Int J Fract*. 2019;215(1-2):1-37.
30. Zienkiewicz O, Taylor R. *The Finite Element Method for Solid and Structural Mechanics*. 6th ed. Butterworth-Heinemann; 2005.
31. Tessler A, Dong SB. On a hierarchy of conforming Timoshenko beam elements. *Comput Struct*. 1981;14(3-4):335-344.
32. Rakowski J. The interpretation of the shear locking in beam elements. *Comput Struct*. 1990;37(5):769-776.

33. Jelenić G, Papa E. Exact solution of 3D Timoshenko beam problem using linked interpolation of arbitrary order. *Arch Appl Mech*. 2011;81(2):171-183.
34. Dukić EP, Jelenić G. Exact solution of 3D Timoshenko beam problem: problem-dependent formulation. *Arch Appl Mech*. 2014;84(3):375-384.
35. Ribarić D, Jelenić G. Higher-order linked interpolation in quadrilateral thick plate finite elements. *Finite Elem Anal Des*. 2012;51:67-80.
36. Ribarić D, Jelenić G. Higher-order linked interpolation in triangular thick plate finite elements. *Eng Comput*. 2014;31(1):69-109.
37. Škec L, Alfano G, Jelenić G. On Gc, Jc and the characterisation of the mode-I fracture resistance in delamination or adhesive debonding. *Int J Solids Struct*. 2018;144-145:100-122.
38. Nian G, Li Q, Qiang X, Shaoxing Q. A cohesive zone model incorporating a Coulomb friction law for fiber-reinforced composites. *Compos Sci Technol*. 2018;157:195-201.
39. Liu W, Chen P. A simple procedure for the determination of the cohesive law in 4-ENF test with consideration of the friction and R-curve effect. *Eng Fract Mech*. 2019;220:106651.
40. Venzal V, Morel S, Parent T, Dubois F. Frictional cohesive zone model for quasi-brittle fracture: mixed-mode and coupling between cohesive and frictional behaviors. *Int J Solids Struct*. 2020;198:17-30.
41. BS ISO 15114. Fibre-reinforced plastic composites - Determination of the mode II fracture resistance for unidirectionally reinforced materials using the calibrated end-loaded split (C-ELS) test and an effective crack length approach. Technical report, British Standards Institution, London; 2014.
42. Ribarić D. *Higher-Order Linked Interpolation in Moderately Thick Plate and Facet Shell Finite Elements*. PhD thesis. Civil Engineering Faculty of Rijeka University, Rijeka, Croatia; 2012.
43. Do BC, Liu W, Yang QD, Su XY. Improved cohesive stress integration schemes for cohesive zone elements. *Eng Fract Mech*. 2013;107:14-28.
44. Taylor RL. FEAP - finite element analysis program; 2017. http://www.ce.berkeley/feap
45. Alfano M, Furgiuele F, Pagnotta L, Paulino GH. Analysis of fracture in aluminum joints bonded with a bi-component epoxy adhesive. *J Test Eval*. 2011;39(2):1-8.
46. Álvarez D, Blackman BRK, Guild FJ, Kinloch AJ. Mode I fracture in adhesively-bonded joints: a mesh-size independent modelling approach using cohesive elements. *Eng Fract Mech*. 2014;115:73-95.
47. Kaleel I, Carrera E, Petrolo M. Progressive delamination of laminated composites via 1d models. *Compos Struct*. 2020;235:111799.
48. Ben Salem N, Jumel J, Budzik MK, Shanahan MER, Lavelle F. Analytical and experimental investigations of crack propagation in adhesively bonded joints with the Mixed Mode Bending (MMB) test Part II: investigation of cohesive stresses distribution with backface strain monitoring. *Theor Appl Fract Mech*. 2014;74:222-232.
49. BS ISO 25217. Adhesives - determination of the mode I adhesive fracture energy of structural adhesive joints using double cantilever beam and tapered double cantilever beam specimens. British Standard, British Standards Institution; 2009.
50. Škec L, Alfano G, Jelenić G. Enhanced simple beam theory for characterising mode-I fracture resistance via a double cantilever beam test. *Compos B*. 2019;167:250-262.
51. Mi Y, Crisfield MA, Davies GAO, Hellweg HB. Progressive delamination using interface elements. *J Compos Mater*. 1998;32(14):1246-1272.

How to cite this article: Ranjbar M, Škec L, Jelenić G, Ribarić D. Mixed-mode delamination of layered structures modeled as Timoshenko beams with linked interpolation. *Int J Numer Methods Eng*. 2023;124(8):1773-1797. doi: 10.1002/nme.7187